Specific forward/reverse latent heat and martensite fraction measurement during superelastic deformation of nanostructured NiTi wires

Henrique Martinni Ramos de Oliveira, Hervé Louche, Estephanie Nobre Dantas Grassi, Denis Favier

Specific forward/reverse latent heat and martensite fraction measurement during superelastic deformation of nanostructured NiTi wires

Henrique Martinni Ramos de Oliveira[a], Hervé Louche[b], Estephanie Nobre Dantas Grassi[a], Denis Favier[a,*]

[a] *Univ. Grenoble Alpes, CNRS, Grenoble INP, TIMC-IMAG, F-38000 Grenoble, France*
[b] *Univ. de Montpellier, F-34090 Montpellier, France*

Abstract

This study analyses the thermomechanical tensile behaviour of a cold drawn Ti-50.9at.%Ni wire submitted to heat treatment at 598 K for 30 min, which is below the recrystallization temperature (623 K). Such low temperature heat treatment induces a superelastic loop without a stress "plateau". However, the absence or weakness of peaks on its differential scanning calorimetry prevents the determination of specific latent heat. This is a common effect of nanostructured materials such as superelastic wires. A method using strain and temperature field measurements was developed and used to determine thermal power and thermal energy during superelastic tensile tests through a heat balance. From these results and using a thermodynamic approach, forward and reverse specific latent heat and the martensite fraction are estimated as a function of strain and stress.

Keywords: superelastic NiTi, nanostructured NiTi wires, kinematic and thermal full field measurements, heat balance, enthalpy of transformation

1. Introduction

Superelastic NiTi wires are manufactured by a sequence of hot [1] and cold drawing [2, 3] which jointly induces an amorphous phase and highly strained

*Corresponding author
Email address: denis.favier@univ-grenoble-alpes.fr (Denis Favier)

nanocrystals in the material.

Usual industrial NiTi wires are subjected to an additional high temperature heat treatment (straight annealing) of around 750-800 K. Such heat treatment promotes grain growth and crystallization of the microstructure [4, 5, 6, 7]. During heating and cooling, a martensite to austenite and an austenite to martensite transformation occurs, respectively, and a significant amount of latent heat is released or absorbed. This latent heat is commonly quantified using the differential scanning calorimetry (DSC) technique, where heat release/absorption is identified by the presence of peaks in the DSC results. Furthermore, when these annealed wires are cyclically stretched they are capable of major reversible deformation associated with a reversible stress-induced phase transformation (SIPT). This effect is known as superelasticity, due to its reversible nature. Superelastic tensile deformation of straight annealed NiTi wires is accompanied by stress plateaus during loading (forward transformation) and unloading (reverse transformation) and exhibits high stress hysteresis. Besides, the deformation along the wire within these plateaus is not uniform at the scale of the wire dimension [8].

On the other hand, cold worked wires can be subjected to additional heat treatments at lower temperatures (473 K to 598 K). In this case, though, DSC tests generally show inconclusive results regarding the quantification of latent heat, since either a weak thermal peak, or even no thermal peak is observed [9, 10, 11, 12, 13]. This does not mean, however, that phase transformation has not taken place. Many authors showed that such wires exhibit the superelastic effect, although their stress-strain curve does not present a stress plateau and a smaller stress hysteresis is observed compared to straight annealed materials [14, 12, 9]. The absence of a stress plateau is associated with a homogeneous strain distribution during deformation.

Knowledge of the amount of latent heat of phase transformation is mandatory in many applications, such as those using the elastocaloric effect of NiTi alloys in cooling devices [15, 16]. These devices make use of the latent heat of SIPT to perform temperature changes in designed systems. Working as heat

pumps, the phase transformation must be induced cyclically to maintain the cooling effect, and the need for cyclic loading/unloading means that the transforming material must have long fatigue life.

In this scenario, the mechanical behaviour of cold worked NiTi alloys heat treated at low temperature is quite suitable: the absence of stress plateaus, and therefore of localization phenomenon, is associated with a longer fatigue life, since localization induces locally high strain [8, 17]. The drawback, however, is that alloys often show inconclusive DSC results, which is a barrier to determine the transformation latent heat, ultimately hindering the use of this material in the design of elastocaloric applications.

To overcome this issue, latent heat of phase transformation can be estimated through an analysis of temperature variation during a SIPT. Using a thermal approach, the involved heat sources can be determined. A method to estimate heat sources from temperature fields measured with an infrared thermal camera was presented by [18]. The same method was used to investigate the heat source of phase transformation [19] and the deformation mechanisms [8] of NiTi tubes.

This study aims to quantify the heat sources generated during a SIPT of a cold worked wire heat treated at 598 K for 30 min. For this purpose, temperature fields are acquired using an infrared thermal camera. This method for heat source quantification using infrared technique was validated by authors in [19, 20, 21] in a NiTi tube and plate showing typical DSC results, i.e. well-defined transformation peaks. Strain fields are acquired using a visible camera and digital image correlation (DIC). Using a thermodynamic framework based on the Gibbs free energy, the specific latent heat of forward and reverse transformations are determined. The specific latent heat obtained are compared with values found in the literature for fully annealed NiTi alloys with similar composition when tested using purely thermal methods (i.e. DSC). Moreover, the martensite fraction is estimated and presented as a function of strain and stress.

2. Material and experimental procedure

2.1. Material

The material used in the experiments campaign is a cold drawn NiTi wire provided by Fort Wayne Metals (NiTi#1) with a composition Ti-50.9at.%Ni. The manufacturer stated that these wires were cold-drawn to a cross section reduction of 47.5%. This cold drawn wire is similar to the wire of diameter 0.1 mm used by Delville et al. [2] and Malard et al. [22, 23] but with a diameter of 0.5 mm. This larger diameter was chosen to allow temperature and strain field measurements during the tensile tests, as described in Section 2.3. Malard et al. [22, 23] observed that this wire in the as-drawn state "possesses a heavily deformed microstructure consisting of a mixture of austenite, martensite and amorphous phases with defects and internal stress". Ahadi and Sun [24, 9] studied a sheet with the same composition (Ti-50.9at.%Ni) than the wire used in this paper. The sheet was cold rolled to achieve 42% thickness reduction. In the cold rolled state, they measured a grain size of 10 nm. The papers of Malard et al. [22, 23] and Ahadi and Sun [24, 9] are in agreement with the review paper of Prokoshin et al. [25] who summarized that the structure is mainly nanosubgrained for low-to-moderate cold work (deformation intensity between 30 and 50%) and mixed (nanosubgrained + nanocrystalline) for moderate to high deformation intensity between 50% and 100%.

In order to improve the functional properties of cold worked structures, post deformation treatment are performed. Ahadi and Sun [9] performed heat treatment of the cold rolled sheets in a furnace at temperatures between 480°C and 520°C for short times (2 to 6 minutes) or at lower temperature (250°C) for 45 minutes [24]. Delville et al. [2] and Malard et al. [22, 23] used a non-conventional heat treatment by controlled electric pulse current to modify the functional properties of the studied 0.1 mm wire. Delobelle et al. [26] performed similar electropulse heat treatment using the 0.5 mm wire studied in the present paper. In our study, a conventional furnace with a temperature controlled with an accuracy of ±1°C was used, with temperature range between 523 K and 598

K and treatment time of 30 minutes.

Figure 1a shows cyclic tensile tests performed at room temperature (297 K) on wires heat treated at 523 K, 548 K, 573 K and 598 K for 30 min. The deformations of the four heat treated wires are fully recoverable. The stress-strain curves do not show any plateau and the hardening is decreasing with increasing heat treatment temperature. The mechanical behaviour of the heat treated wires is similar to the results obtained by [23] (Fig. 6) using heat treatment by pulsed DC electric current of pulse duration between 6 and 10 ms. They are also in agreement with results obtained by Ahadi and Sun [24] and [9] for Ti-50.9at.%Ni sheet heat treated at temperatures between 485°C and 520°C for short time (2 or 3 minutes) or at lower temperature (250°C) for 45 minutes. Ahadi and Sun [9] and Malard et al. [22, 23] performed TEM observation and X-ray diffraction measurements on their samples. They observed that isothermal stress-strain curves without stress plateau were obtained for grain sizes between 10 and 70 nm [9] and between 10 and 40 nm [22]. Malard et al. [22] also observed that after treatments with pulse times of 6-10 ms, amorphous regions are no more observed and samples are in austenitic state at room temperature with polygonised microstructures.

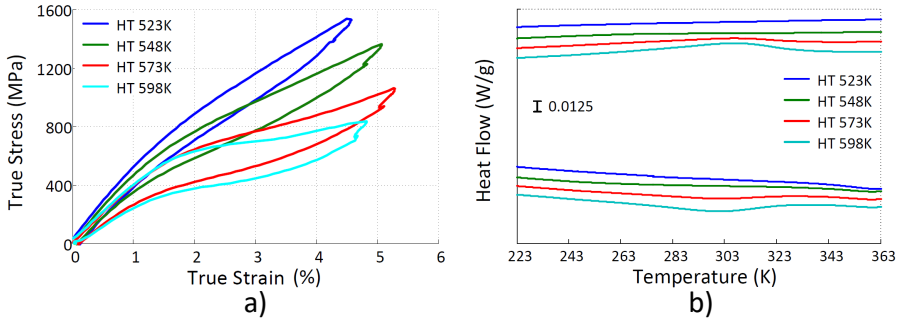

Figure 1: *a) Tensile response at room temperature (297 K) for different heat treatment temperatures. b) DSC results for the wires with the different heat treatments (the curves are plotted with an offset of 0.0125 W/g).*

Figure 1b shows the DSC result of the heat treated wires. A Q200 DSC test-

ing machine from TA Instruments was used and the tests were carried out with a temperature rate of ±10 K/min between 223 K and 363 K. Transformation behavior of wires heat treated at 523 K and 548 K are flat and do not exhibit any peak. This result is in agreement with Ahadi and Sun [9] (Fig. 2) for grain size lower than 30 nm. Transformation peaks well spread over a large temperature range are observed for samples heat treated at 573 K and 598 K. A difference around 10 K between heating and cooling "peak temperatures" is the signature of the austenite to R phase transformation. However, the heat measured during cooling and heating are of the order of 1.0 J/g and 1.7 J/g for heat treatment temperature of 573 K during cooling and heating, respectively and of the order of 1.2 J/g for cooling and 1.6 J/g for heating, for heat treatment temperature of 598 K. Such low heat values obtained from DSC curves are even lower than normal values obtained for R-phase transformation, that are in the order of 6 J/g [27]. These results put in evidence the difficulty of obtaining the heat of phase transformation for these heat treatment temperature through DSC tests.

In the following, only the wire heat treated at 598 K will be studied to present the method to determine thermal power and energy, forward and reverse specific latent heat and martensite fraction. Isothermal stress-strain curves at room temperature (297 K) will be analyzed.

2.2. Superelastic tensile tests

The NiTi wire sample was mounted on a standard gripping system on a tensile testing machine (Gabo Qualimeter) equipped with a 500 N load cell. The gauge length of the sample was $L_0 = 20$ mm. Before clamping, the wire was heated in boiling water and then cooled down to room temperature. This procedure was conducted to start the test with the highest possible austenite fraction. The heat measured during cooling in the DSC of Fig. 1b is 1.2 J/g for the whole peak and 0.5 J/g at 297 K, the tensile test temperature. This means that, in agreement with Mallard et al. [22, 23], the wire at the beginning of the tensile test is austenitic with polygonised microstructure having a small amount of R-phase, estimated to be less 10% considering a latent heat of 6 J/g

for a full A-R-phase.

The tensile test was performed by loading and unloading the NiTi wire at a pre-set global strain of 6% with a strain rate of $10^{-2}s^{-1}$. During the load-unload cycle, two hold-times were performed: one at the end of loading and one at the end of unloading, for 50 s each. The purpose of the hold times was to allow the wire to achieve room temperature after forward and reverse phase transformations. In addition, the wire was submitted to a tensile test until rupture using the same strain rate.

2.3. Thermal and kinematic full field measurements during tensile tests

The temperature field was measured with a fast multi-detector infrared camera (FLIR SC6000 series), with a resolution of 640 x 512 pixels equipped with a medium wavelength infrared (MWIR) macro 1:3.0 objective lens. The spatial resolution (pixel size) was 16 μm $\times$ 16 μm. The surface of the wire observed by the IR camera was coated with a highly emissive black paint in order to obtain black body properties compatible with the infrared camera calibration. The thermal field was measured in sections of length $l_0 = 8.2$ mm, shorter than L_0 (see Fig. 2). There were 31 pixels in the radial direction of the wire and the size of the IR zone of interest (ZOI) was then 512 x 31 pixels.

The displacement field was obtained using a visible-light digital camera (ALLIED, 2048 x 2048 pixels) and VIC 2D Digital Image Correlation processing software. The visible camera recorded the side of the wire opposite the IR zone. The surface on this side was covered with a random pattern of white paint speckles over a black paint coat to allow displacement and strain field measurements through image correlation. The resolution of the visible light camera ZOI was 2048 x 72 pixels. However, the ZOI used to perform the DIC analysis was 1181 x 72 pixels, which corresponds to the same length $l_0 = 8.2$ mm filmed by the thermal camera. In this ZOI, a subset of 25 pixels with a step of 17 pixels led to a spatial resolution of $\sim$ 0.17 mm in the axial direction and $\sim$ 0.12 mm in the circumferential direction. From that, the strain profiles obtained were calculated taking only the axial component ε_{yy} of the true logarithmic strain

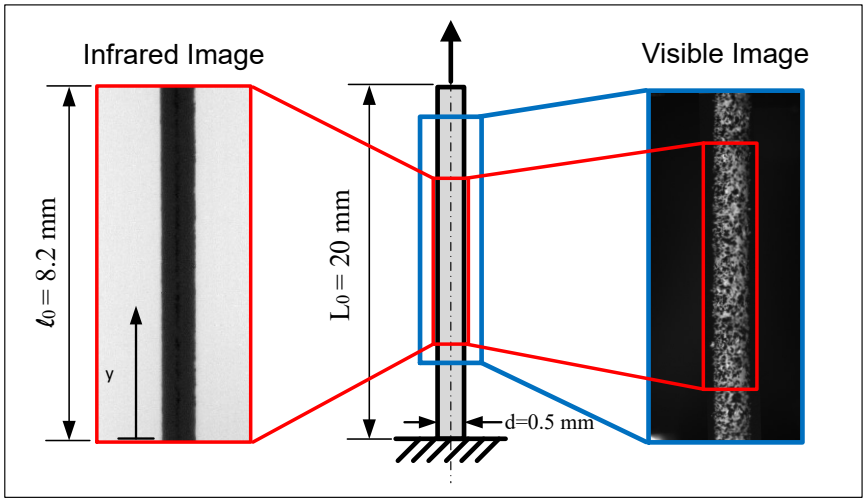

Figure 2: *Experimental set-up showing the NiTi wire in the center with extracted thermal and visible images.*

tensor into account.

In the following, the true strain ε_{yy} is named ε for simplification and the average value in the ZOI $\langle\varepsilon\rangle$. The uniform temperature variation, computed as the difference between the average absolute temperature in the IR ZOI $\langle T\rangle$ and the room temperature T_0, is named $\langle\theta\rangle$, i.e. $\langle\theta\rangle = \langle T\rangle - T_0$.

From the full field measurements it was possible to obtain the results in Fig.3. The loading stress-average strain $\langle\varepsilon\rangle$ behaviour of the superelastic NiTi wire is shown in Fig. 3a. Each colored marker represents the strain levels in which the strain profiles in Fig. 3b and the temperature variation profiles in Fig. 3c are plotted. The curves shown in Fig. 3b indicate a uniform strain behaviour of the NiTi wire, with no strain localization phenomenon [9, 28]. This behaviour is ratified by the results in Fig. 3c, where the temperature variation profiles over the wire length are also uniform. These observations justify working with average values $\langle\theta\rangle$ and $\langle\varepsilon\rangle$.

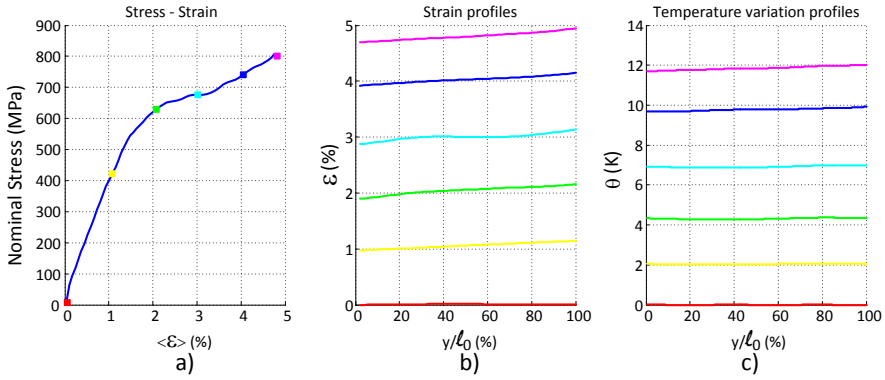

Figure 3: *a) Tensile stress-strain curve during loading of the NiTi wire, where $\langle\varepsilon\rangle$ is the average logarithmic strain measured with DIC over the length l_0, defined in Fig. 2. b) Logarithmic strain profiles over the wire gauge length at different strain levels, as indicated by the colored markers in (a). c) Temperature variation profiles at different strain levels.*

2.4. Heat sources and thermal energy estimation

In the present study, due to the uniform temperature variation along the tested wire, a time dependent thermal approach was chosen. The thermal framework used to estimate heat sources during a superelastic tensile test is presented hereafter.

For a simple geometry (wire) with uniformly distributed heat sources, and also if the specimen is not too far from thermal equilibrium with the ambient medium at T_0, the thermal model reads [29, 18, 27]:

$$c\left(\frac{\partial\langle\theta\rangle}{\partial t}+\frac{\langle\theta\rangle}{\tau_{eq}}\right)=\langle\dot{q}\rangle \tag{1}$$

where $\langle\dot{q}\rangle$ represents the uniform heat source or thermal power per mass unit, c the specific heat and τ_{eq} a characteristic time.

As shown by [29, 18], the heat source in the right member of Eq.1 can be calculated from experimental data. It is obtained from estimations of the two terms of the left member after some filtering and numerical derivative operations.

The uniform heat sources are denoted $\dot{q}$ for simplification. The specific heat c is assumed to be uniform and constant. The parameter τ_{eq} represents a characteristic time of heat loss by both convection and radiation through the specimen surface and by conduction towards the grip zone.

Thermal energy E_{th} is calculated though time integration of the heat sources per unit of mass $\dot{q}$:

$$E_{th}(t) = \int_0^t \dot{q} dt \tag{2}$$

2.5. Determination of mechanical power and energy

Mechanical power P_{mech} and mechanical energy E_{mech} are both determined per unit of mass. P_{mech} is defined as:

$$P_{mech} = \frac{\sigma \dot{\varepsilon}}{\rho} \tag{3}$$

where σ is the uniaxial tensile true stress, $\dot{\varepsilon}$ is the uniaxial strain rate and ρ the mass density. True stress σ is calculated from $\sigma = \sigma_0(1 + \varepsilon_n)$, where σ_0 is the engineering stress and ε_n is the nominal strain.

The mechanical energy per unit of mass E_{mech} is calculated by time integration of the mechanical power:

$$E_{mech}(t) = \int_0^t P_{mech} dt \tag{4}$$

3. Results

3.1. Strain and temperature field variation

Figure 4 shows the nominal stress-true strain $\sigma_0 - \langle\varepsilon\rangle$ curve of the uniaxial tensile test (Fig. 4a). The time course of the temperature variation $\langle\theta\rangle$ and strain $\langle\varepsilon\rangle$, both considered uniform, are shown in Fig. 4b. This figure also shows the strain rate time evolution $\langle\dot{\varepsilon}\rangle$, calculated by numerical derivation of the strain time evolution.

Four distinct stages are outlined, denoted I$(0 - a)$, II$(a - b)$, III$(b - c)$ and IV$(c - d)$:

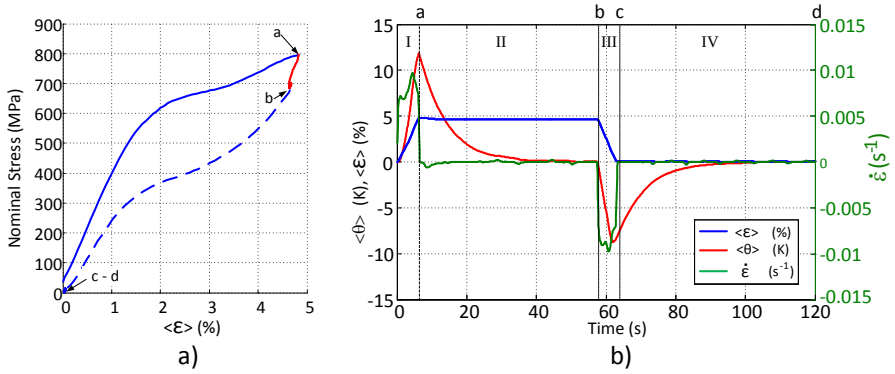

Figure 4: *a) Stress-strain curve for a single cycle tensile test at* $\langle\dot{\varepsilon}\rangle = 10^{-2}s^{-1}$. *b) Average temperature variation* $\langle\theta\rangle$*, average strain and average strain rate over a time course.*

- Stage I: The temperature increases as the strain increases to 4.8%. Due to the fast release of the latent heat of phase transformation, the temperature increase was $\theta = 11.8$ K.
- Stage II: The first hold time allows the temperature to decrease to T_0 while $\langle\dot{\varepsilon}\rangle \approx 0$ and $\langle\varepsilon\rangle$ remains almost constant.
- Stage III: The strain recovery promoted the absorption of latent heat due to reverse transformation, leading to a negative temperature variation of $\langle\theta\rangle = -8.7$ K. At the end of stage III (end of unloading), the temperature starts to increase again just before the strain reaches zero.
- Stage IV: The second hold time allows the temperature to increase to T_0 while $\langle\dot{\varepsilon}\rangle = 0$ and $\langle\varepsilon\rangle$ remains constant.

3.2. Estimation of thermal power

The average thermal power $\dot{q}$ was calculated using the average temperature $\langle\theta\rangle$ shown in Fig. 4b and Eq. 1 with $c = 500$ J kg^{-1}K^{-1} [27].

Figure 5a shows the temperature variation $\langle\theta\rangle$ and an example of the time evolution of the thermal power ($\dot{q}$) computed with a value of $\tau_{eq} = 5$ s. From this example of thermal power estimation, we observed that the best value of

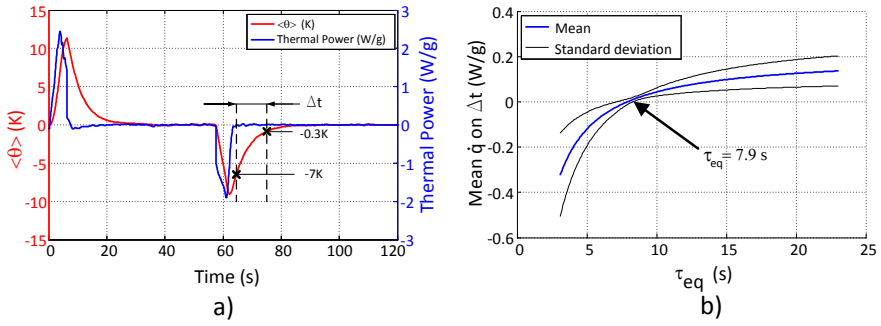

Figure 5: *a) Uniform temperature variation $\langle\theta\rangle$ and thermal power $\dot{q}$, presented on left and right axis, respectively, as a function of time. b) Mean and standard deviation of $\dot{q}$, calculated in the time interval Δt shown in a), obtained for different τ_{eq} values.*

τ_{eq} could be calculated on the hold-time of stage IV, where no thermal energy is being released or absorbed, since no phase transformation is taking place.

For imposed τ_{eq} values and using Eq. 1, thermal power $\dot{q}$ was computed on the time interval Δt. In Figure 5b, the thick blue line represents the mean value of $\dot{q}$ as a function of τ_{eq}, and the black lines are the limits of the standard deviation. With this procedure, the $\tau_{eq} = 7.9$ s value was determined, which optimally leads to a thermal power close to zero during stage IV. The $\tau_{eq} = 7.9$ s value was used in the further calculations of thermal power and thermal energy.

3.3. Thermal and mechanical power and energy as a function of time

Figure 6 shows the thermal and mechanical power per unit of mass (W/g) and the thermal E_{th} and mechanical E_{mech} energy per unit of mass (J/g), both as a function of time. Similarly to Fig. 4b, four stages are outlined in Fig. 6.

From the power curves, the following observations are made:

- Stage I: The thermal power increases suddenly until it reaches a peak at approximately $\dot{q} = 2.1$ W/g. The same qualitative behaviour is observed for the mechanical power, which simultaneously reaches a maximum at $P_{mech} = 1.0$ W/g. After the thermal peak in stage I, the decrease in

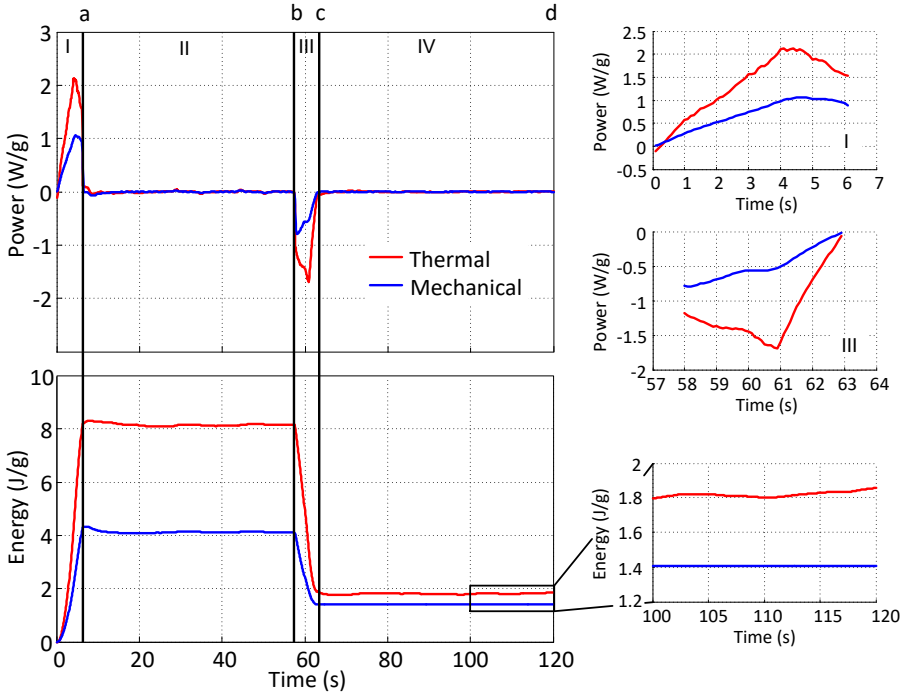

Figure 6: *Thermal and mechanical power and energy per unit of mass as a function of time for a single superelastic tensile test at* $\dot{\varepsilon} = 10^{-2}\ s^{-1}$. *On the right, close-ups of stages I and III of power curves and of energy curves at the end of stage IV.*

thermal power highlights the decrease of the phase transformation activity before the end of loading.

- Stage II: During the first hold time, the thermal power is close to zero, except at the beginning, where the thermal power is slightly negative.

- Stage III: Reverse martensite transformation takes place. The thermal power shows the same qualitative response as in stage I (loading) but with a peak at $\dot{q} = -1.7$ W/g. Despite its lower amplitude compared to loading, it is around twice as large as the mechanical power, which reaches $P_{mech} = -0.8$ W/g.

- Stage IV: During the second hold time, the thermal power is zero.

From the energy curves, the following observations are made:

- Stage I: During loading there is a monotonic increase in thermal and mechanical energy, reaching a maximum of $E_{th} = 8.3$ J/g and $E_{mech} = 4.3$ J/g, respectively.

- Stage II: At the beginning of the first hold-time, there is a slight drop in the energy level for both thermal and mechanical energy. Then the energy tend to a constant level, once no power is generated during this stage.

- Stage III: During unloading, there is a decrease in thermal and mechanical energy. This is due to the endothermic reverse transformation and to the strain recovery.

- Stage IV: The energy levels at the end of stage III remain constant during the second hold-time. The mechanical energy, which is equivalent to the hysteresis area on the stress-strain curve, is $E_{mech} = 1.4$ J/g. The thermal energy during this stage is close to the mechanical energy, i.e. around $E_{th} = 1.8$ J/g. The minor difference between both energies, which is of the order of experimental error [30], suggests that a thermodynamic cycle is performed. A similar result was obtained by [31] for a CuZnAl alloy.

3.4. Thermal and mechanical power and energy as function of strain and stress

3.4.1. Cyclic test

Power

Figure 7 shows, in a function of true strain $\langle\varepsilon\rangle$, the thermal ($\dot{q}$) and mechanical ($P_{mech}$) power per unit of mass (on the left ordinate axis) and strain rate ($\dot{\varepsilon}$) (on the right ordinate axis). The dots represent the loading and the empty circles represent the unloading.

The thermal power increases from the beginning of loading. The non-zero values at low strain levels confirm that phase transformation begins early in stage I. The increase stops at approximately 3% strain. Beyond this point, thermal power decreases slightly until the end of unloading. This behaviour suggests

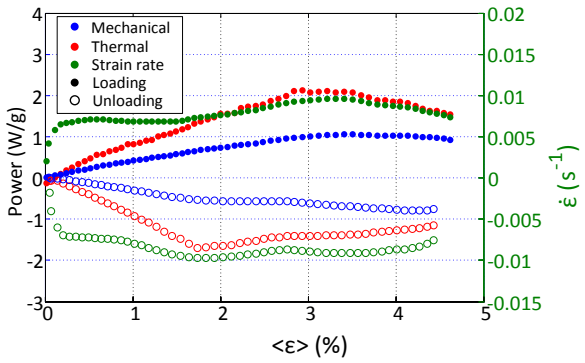

Figure 7: *Evolution, with strain, of thermal and mechanical power per unit of mass (left ordinate axis) and strain rate (right ordinate axis), on loading (dots) and unloading (empty circles).*

a decrease in thermal activity, possibly due to a decrease in the phase transformation rate. The same trend is observed regarding the mechanical power. Thermal power starts to decrease from the beginning of unloading. It reaches its minimum around 1.7% strain. Mechanical power, however, shows a monotonically decreasing response, starting at 4.5%. The recoverable nature of this phenomenon is qualitatively revealed as an almost symmetrical load-unload path.

As shown in Fig. 7, the strain rate was not constant during the test. This variation was most likely due to fact that the test was performed with a constant machine crosshead speed. Actual strain rate was measured locally by DIC. Hence, any sample slip and/or accommodation of grips set-up may have caused the observed variation in the strain rate. Thus, thermal and mechanical powers were normalized by the strain rate measured by DIC to avoid misleading interpretations due to strain rate variations.

The normalized powers are plotted in Figs. 8a and 8b as a function of strain and stress, respectively. The normalized thermal power in Fig. 8a shows the same qualitative response presented in Fig. 7. From this observation, the strong presence of phase transformation is noted from 0 to 3% strain, as well as its weakening from 3% strain until the end of loading.

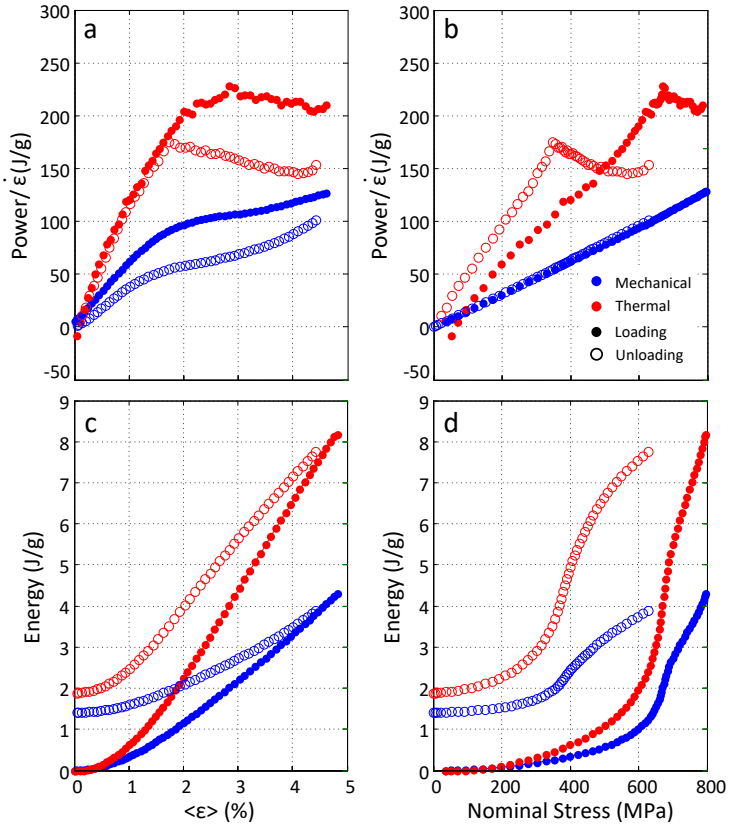

Figure 8: *Thermal and mechanical power normalized by the strain rate in function of (a) true strain and (b) nominal stress; and thermal and mechanical energy normalized by the strain rate in function of (c) true strain and (d) nominal stress.*

Analogously, in Fig. 8b the thermal power peak takes place around 700 MPa on loading, which is approximately the end of superelastic "plateau" (zone where the phase transformation is more pronounced) observed in Fig. 4a. During unloading, the thermal peak appears at approximately 350 MPa, which is the end of the unloading "plateau" on the stress-strain curve shown in Fig. 4a.

Energy

Figure 8c and d shows thermal and mechanical energy per unit of mass as a function of strain and stress. In Fig. 8c, mechanical energy increases mono-

tonically until 4.3 J/g at the end of loading and decreases continuously to 1.4 J/g at the end of unloading. Thermal energy also shows the same qualitative behaviour, although it reaches 8.3 J/g at the end of loading, about twice the magnitude of the mechanical energy. During unloading, thermal energy decreases, reaching a minimum at 1.8 J/g, around to lowest mechanical energy level.

In Fig. 8d, at loading, thermal energy increases to 2 J/g in the range of 0 to 600 MPa. With further loading, from 600 MPa to 800 MPa, it increases from 2 J/g to 8.3 J/g. The same qualitative behaviour is observed for the mechanical energy, where most of the energy is released in the zone where the stress is more constant on the stress-strain curve.

3.4.2. Rupture test

Figure 9 shows the normalized power and energy as a function of true strain for the tensile test until rupture. The curves in Fig. 9a have the same qualitative behaviour as in the cyclic tensile test in Fig. 8a: an increasing monotonic thermal response reaching a maximum at approximately 3% strain, followed by a decrease. During the rupture tests, the decrease continues until approximately 10% strain. Then a slight increase in the normalized thermal power is observed before rupture.

In the same manner, Figure 9b shows the qualitative behaviour observed in Fig. 8c regarding thermal and mechanical energy. A maximum of 19.3 J/g is reached by thermal energy while the mechanical energy reaches 15.3 J/g at the end of the test. However, due to the presence of plastic deformation, the energy levels cannot be exclusively associated with phase transformation.

4. Discussion

4.1. Deformation mechanisms in SMA

Deformation mechanisms in NiTi alloys include elastic strain and martensitic transformation [32]. Plastic deformation may be involved but is only effective

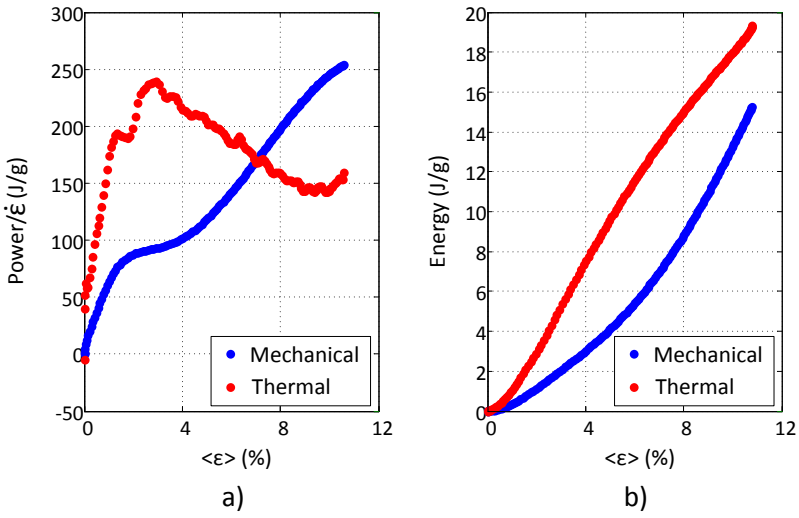

Figure 9: *a) Thermal and mechanical power normalized by the strain rate as a function of true strain. b) Thermal and mechanical energy as a function of true strain.*

at high strain [33]. The additive decomposition of the total strain rate ($\dot{\varepsilon}$) is thus assumed to be:

$$\dot{\varepsilon} = \dot{\varepsilon}_{el} + \dot{\varepsilon}_{in} = \dot{\varepsilon}_{el} + \dot{\varepsilon}_{tr} + \dot{\varepsilon}_{pl} \tag{5}$$

where $\dot{\varepsilon}_{el} = \dot{\sigma}/\mathrm{E}$ and $\dot{\varepsilon}_{in}$ are the elastic and inelastic strain rates, respectively, and E is the Young modulus. The inelastic strain rate ($\dot{\varepsilon}_{in}$) includes the strain rate due to phase transformation ($\dot{\varepsilon}_{tr}$) and to plasticity ($\dot{\varepsilon}_{pl}$).

In this study, the Young modulus is E = 70 GPa. This value, measured by dynamic mechanical analysis, is the same for austenite and oriented martensite [34].

Analogously, the thermal power is decomposed as in Eq. 6:

$$\dot{q} = \dot{q}_{thel} + \dot{q}_{in} = \dot{q}_{thel} + \dot{q}_{tr} + \dot{q}_{pl} \tag{6}$$

where the thermoelastic heat source is $\dot{q}_{thel} = -(\alpha T_0/\rho)\dot{\sigma}$, calculated with the

coefficient of thermal expansion $\alpha = 1.1 \times 10^{-5}$ K^{-1} [27], T_0 is the test temperature, $\rho = 6500$ kg m^{-3} is the volumic mass and $\dot{\sigma} = d\sigma/dt$ is the true stress rate; $\dot{q}_{in}$ is the inelastic thermal power, $\dot{q}_{tr}$ is the heat source associated with phase transformation and $\dot{q}_{pl}$ is associated with the dissipated power due to plasticity.

Lastly, the mechanical power per unit of mass can be decomposed as in Eq. 7:

$$P_{mech} = P_{mech\_el} + P_{mech\_in} \tag{7}$$

where the elastic and inelastic mechanical power per unit of mass are: $P_{mech\_el} = \frac{1}{\rho}\sigma\dot{\varepsilon}_{el}$ and $P_{mech\_in} = \frac{1}{\rho}\sigma\dot{\varepsilon}_{in}$, respectively.

Furthermore, thermal and mechanical energy are also decomposed into elastic and inelastic portions, as described before. They are calculated through time integration of their respective power components.

4.2. Impact of thermoelasticity on thermal power and energy

An analysis of the cyclic test results described in section 3.4.1 is proposed in this section. Thermal power ($\dot{q}/\dot{\varepsilon}$) and inelastic thermal power ($\dot{q}_{in}/\dot{\varepsilon}$), both normalized by strain rate, are plotted on the left ordinate axis in Fig. 10. Variations in the ratio between inelastic thermal power and mechanical power ($\dot{q}_{in}/P_{mech\_in}$) are indicated in the right axes. These quantities are plotted in Fig. 10a and Fig. 10b, respectively.

The normalized inelastic thermal power ($\dot{q}_{in}/\dot{\varepsilon}$) is slightly higher than the thermal power ($\dot{q}/\dot{\varepsilon}$). This difference is clearer at the beginning of loading, i.e. between $0-2\%$ in Fig. 10a and 0-600 MPa in Fig. 10b. These ranges represent the portion of the superelastic loop where the elasticity is the most important strain component.

The limits of these ranges also correspond to the change of slope on the stress-strain curve plotted in Fig. 3a. The thermal power at the beginning of loading (up to 0.1% strain or 50 MPa) is negative. Endothermic heat sources due to thermoelastic coupling could explain such negative thermal power. Thereafter, and before the end of the initial constant stress-strain slope, the thermal

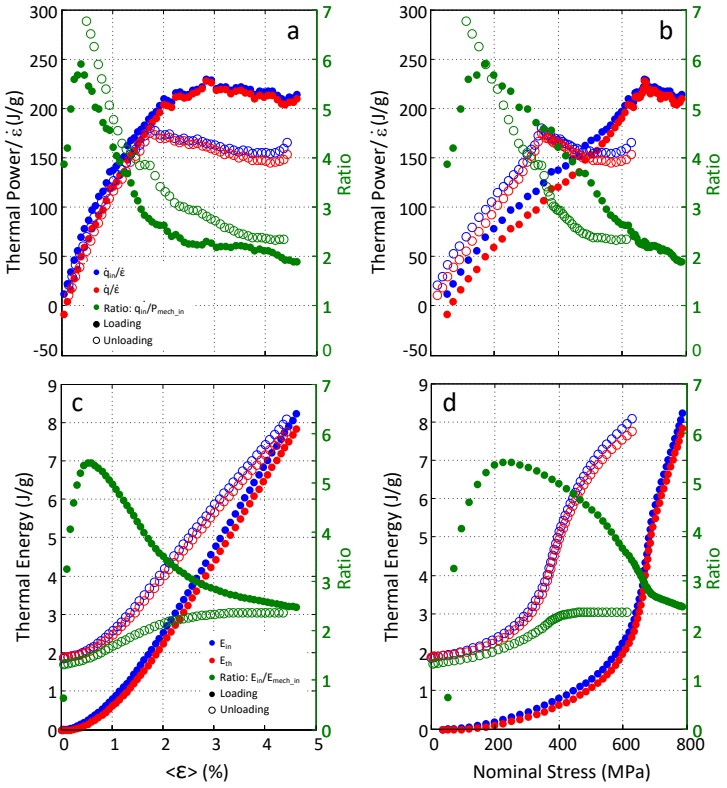

Figure 10: *Normalized inelastic thermal power ($\dot{q}_{in}/\dot{\varepsilon}$) and normalized thermal power ($\dot{q}/\dot{\varepsilon}$) on the left ordinate axes; ratio between inelastic thermal power ($\dot{q}_{in}$) and inelastic mechanical power on right ordinate axes ($\dot{q}_{in}/P_{mech\_in}$) as a function of a) true strain and b) nominal stress. (c) and (d) are organized in the same manner, showing thermal energy (E_{th}), inelastic thermal energy (E_{in}) and energy ratio (E_{in}/E_{mech_in}).*

power is positive, revealing the presence of exothermic heat sources due to phase transformation. When the superelastic "plateau" is reached (between 2-4.8% in Fig. 10a and 600-800 MPa in Fig. 10b) $\dot{q}_{in}$ and $\dot{q}$ are close.

The ratio between inelastic thermal and mechanical power ($\dot{q}_{in}/P_{mech\_in}$) quickly increases to a value close to 6 and then decreases until around 2. During unloading, this ratio changes monotonically from around 2 to 7 at the end of unloading. Such high values imply a significant thermal effect compared to the mechanical power. This ratio, commonly reported in the literature as the Taylor

and Quinney coefficient, is usually less than 1 for plastic deformation of metals or polymers [35, 36, 37]. The thermal and mechanical power ratio greater than 1 could be explained by the presence of deformation mechanisms other than plasticity, i.e. phase transformation in the present case.

Analogously to Figure 10, Figures 10c and 10d present the energy and energy ratio results as a function of strain and stress, respectively. The thermal energy (E_{th}) and the inelastic thermal energy (E_{in}) are on the left ordinate axes. Thermal energy was calculated using Eq. 2 and the data shown in Fig. 6. The evolution of the ratios between inelastic thermal energy and mechanical energy (E_{in}/E_{mech_in}) are on the right axes.

A slight difference between thermal energy (E_{th}) and inelastic thermal energy (E_{in}) is observed and could be explained by the thermoelasticity occurring at the beginning of loading. However, no difference is observed at the end of unloading, highlighting the reversibility of the thermoelastic effect.

For the ratio between inelastic thermal and mechanical energy, a sudden rise from 0 to around 5.5 is observed during loading. Then a decreasing tendency to a ratio of 2.5 is observed. In a similar manner, [38] and [31], studying thermal and mechanical energy of a CuZnAl SMA, reported a ratio of 10.

4.3. Thermodynamics of martensitic transformation

4.3.1. Thermodynamic framework

Several thermodynamic frameworks have been proposed to describe the thermomechanical behaviour of shape memory alloys. This work is based on the approach developed by Ortin and Planes and Wollants et al. [39, 40, 41, 42]. It expresses the martensitic transformation as a diffusionless first order reversible transformation at the scale of an elementary volume. The occurrence of a thermoelastic martensitic transformation is determined by the Gibbs free energy (G) balance at equilibrium, which is given by the condition $dG = 0$. For a thermoelastic martensitic transformation in a polycrystalline matrix, the free energy per unit mass changes over an infinitesimal step of martensite fraction df_m of transformation is expressed as [40, 42]:

$$dG = (\Delta H_c - T\Delta S_c)df_m + \delta E_{st} + \delta E_{fr} - \delta W^{tr}_{mech} = 0 \quad (8)$$

where:

- $dG = (\partial G/\partial f_m)df_m = G'df_m$;
- ΔH_c is the difference between the specific enthalpies of martensite and austenite;
- ΔS_c is the difference between the specific entropies of martensite and austenite;
- f_m is the mass fraction of martensite defined in the elementary volume. It depends only on time and its time derivate $\frac{\mathrm{d}f_m}{\mathrm{d}t}$ is denoted $\dot{f}_m$.
- T is the temperature;
- $\delta E_{st} = (\partial E_{st}/\partial f_m)df_m = E'_{st}(f_m)df_m$ is the stored energy in the elementary volume transformed in the infinitesimal step df_m;
- $\delta E_{fr} = (\partial E_{fr}/\partial f_m)df_m = E'_{fr}(f_m)df_m$ is the friction energy dissipated in the infinitesimal step df_m;
- $\delta W^{tr}_{mech} = (\partial W_{mech}/\partial f_m)df_m = W'_{mech}(f_m)df_m$ is the external mechanical work per unit mass of the elementary volume performed during the infinitesimal step df_m.

All terms in Eq. 8 are algebraic values expressed as energy per unit mass in J/g. The infinitesimal martensite mass fraction step (df_m) is positive during forward transformation and negative during reverse transformation. The term δE_{fr} is the sum of all irreversible energies, such as the energy dissipated through dislocation and interface movement. Moreover, the term δE_{fr} is always dissipated, thus is always positive. E'_{fr} is then positive during forward transformation and negative during reverse transformation. Equation 8 can be rewritten as:

$$\Delta H_c - T\Delta S_c + E'_{st} + E'_{fr} - W'_{mech} = 0 \tag{9}$$

4.3.2. Transformation heat source

The transformation heat source $\dot{q}_{tr}$ is defined as:

$$\dot{q}_{tr} = \dot{q}_{tr\_chem} + \dot{q}_{tr\_diss} = -T\Delta S_c \dot{f}_m + E'_{fr}(f_m)\dot{f}_m = \Delta H_{tr}(f_m)\dot{f}_m \tag{10}$$

where ΔH_{tr} is the specific latent heat and $\dot{q}_{tr\_chem}$ and $\dot{q}_{tr\_diss}$ are the chemical and dissipative parts of $\dot{q}_{tr}$. Assuming that E'_{fr} is totally converted into heat [42], ΔH_{tr} can be written as:

$$\Delta H_{tr} = -T\Delta S_c + E'_{fr} \tag{11}$$

or using Eq. 9

$$\Delta H_{tr} = -\Delta H_c - E'_{st} + W'_{mech} \tag{12}$$

4.3.3. Forward and reverse specific latent heat

Analyzing Eqs. 11 and 12 for a transformation cycle (forward and reverse transformations):

- On loading $(A - M)$, with $\dot{f}_m > 0$:

$$\Delta H_{tr}^{A-M} = -T^{A-M}\Delta S_c + E'^{A-M}_{fr} \tag{13}$$

and

$$\Delta H_{tr}^{A-M} = -\Delta H_c - E'^{A-M}_{st} + W'^{A-M}_{mech} \tag{14}$$

- On unloading $(M - A)$, with $\dot{f}_m < 0$:

$$\Delta H_{tr}^{M-A} = -T^{M-A}\Delta S_c + E'^{M-A}_{fr} \tag{15}$$

and

$$\Delta H_{tr}^{M-A} = -\Delta H_c - E_{st}'^{M-A} + W_{mech}'^{M-A} \tag{16}$$

with

- $\Delta S_c < 0$ and $\Delta H_c < 0$;
- $E_{fr}'^{A-M} > 0$ and $E_{fr}'^{M-A} < 0$;
- $E_{st}'^{A-M} > 0$ and $E_{st}'^{M-A} > 0$;
- $W_{mech}'^{A-M} > 0$ and $W_{mech}'^{M-A} > 0$.

Combining Eqs. 13 and 15:

$$\Delta H_{tr}^{A-M} - \Delta H_{tr}^{M-A} = -(T^{A-M} - T^{M-A})\Delta S_c + (E_{fr}'^{A-M} - E_{fr}'^{M-A}) \tag{17}$$

With the terms $E_{fr}'^{A-M} > 0$ and $E_{fr}'^{M-A} < 0$, the second term on the right hand side of Eq. 17 is always positive. Moreover, as the component ΔS_c is a negative constant, the first term on the right hand side is also positive. However, its magnitude is strongly dependent on the temperature variation.

On the other hand, combining Eqs. 14 and 16 results in:

$$\Delta H_{tr}^{A-M} - \Delta H_{tr}^{M-A} = -(E_{st}'^{A-M} - E_{st}'^{M-A}) + (W_{mech}'^{A-M} - W_{mech}'^{M-A}) \tag{18}$$

The difference in stored energy between loading and unloading ($E_{st}'^{A-M} - E_{st}'^{M-A}$) is very often assumed to be zero since the stored energy is considered to be reversible. From that, the difference in specific latent heat between loading (ΔH_{tr}^{A-M}) and unloading (ΔH_{tr}^{M-A}) can be written as the difference in mechanical work. Then, Eq. 18 is written as:

$$\Delta H_{tr}^{A-M} - \Delta H_{tr}^{M-A} = W_{mech}'^{A-M} - W_{mech}'^{M-A} \tag{19}$$

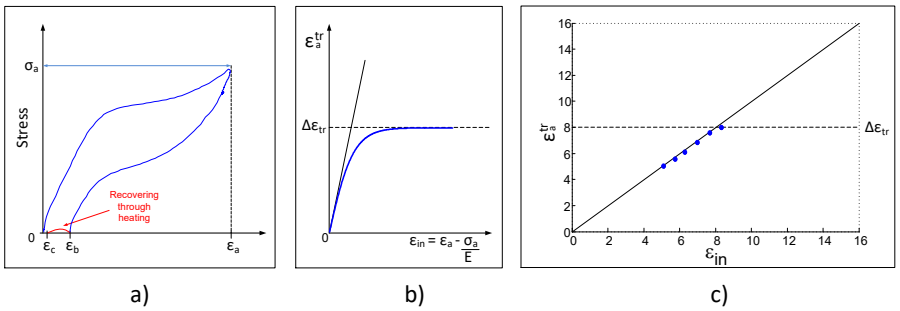

Figure 11: *a) Scheme of a superelastic cycle of SMA showing the residual deformation after loading (ε_a), after unloading (ε_b) and after heating (ε_c). (b) Theoretical evolution of ε_a^{tr} with the inelastic strain ε_{in}. c) Experimental data used to determine the transformation strain $\Delta\varepsilon_{tr}$ value.*

5. Characterisation of the martensitic transformation

5.1. Determination of transformation strain ($\Delta\varepsilon_{tr}$)

To determine the transformation strain $\Delta\varepsilon_{tr}$ several superelastic tensile tests were carried out at different strain levels between 7% and 11%. The tests were performed on a Gabo Qualimeter testing machine with displacement control and crosshead speed of 10^{-5} s^{-1}. The tests consisted of loading the wire (at room temperature) until deformation ε_a, unloading until zero stress, and then heating the wire at 373K.

Figure 11a schematically presents a superelastic cycle with the decomposition of strain. At the end of loading, the total strain ε_a is composed by an elastic strain ε_a^{el}, a plastic strain ε_a^{pl} and a transformation strain ε_a^{tr}. After unloading, a final strain ε_b is achieved. Heating above the finishing temperature of reverse martensitic transformation triggers partial strain recovery, allowing the material to reach the final strain level ε_c.

The strain ε_a is written as:

$$\varepsilon_a = \varepsilon_a^{el} + \varepsilon_a^{in} = \varepsilon_a^{el} + \varepsilon_a^{tr} + \varepsilon_a^{pl} \tag{20}$$

with $\varepsilon_a^{el} = \sigma_a/E$ and ε_a^{in} being the inelastic strain.

Assuming $\varepsilon_a^{pl} = \varepsilon_c$, Eq.20 can be rewrited as:

$$\varepsilon_a^{tr} = \varepsilon_a - \varepsilon_c - \frac{\sigma_a}{E} \tag{21}$$

All values on the right hand side of Eq. 21 can be measured experimentally.

Theoretically, the transformation strain ε_a^{tr} increases with increasing ε_a until a maximum denoted $\Delta\varepsilon_{tr}$, when the phase transformation is complete, i.e. $f_m = 1$. The evolution of ε_a^{tr} with ε_{in} is then assumed to follow a curve similar to that in Fig. 11b.

Figure 11c shows the experimental results of tests carried out using the aforementioned method. In the present study, the tested wires reached rupture before the theoretical asymptotic value. From this figure, a default value of 8% was adopted for $\Delta\varepsilon_{tr}$.

This value is in agreement with that used in two previous studies. The first one was the work published by [43] in which they observed that the $\Delta\varepsilon_{tr}$ of A-M transformation was around 8%. The second is from [44], describing the orientation dependence of the transformation strain $\Delta\varepsilon_{tr}$ in NiTi single crystals. Transmission electron microscopy (TEM) performed in the cold worked and annealed NiTi wires showed a preferred crystallographic orientation along the $\langle 110 \rangle$ direction [30]. From the work of [44], $\Delta\varepsilon_{tr}$ ranges from 8% to 9% in this direction.

5.2. Analyzing the thermomechanical coupling

The equations presented in Sections 4.1 and 4.3 are now used to further analyze thermomechanical coupling during the SIPT.

5.2.1. Strain rate analysis

In the following it is assumed that the deformation mechanism only consists of elasticity and phase transformation. The effects of plasticity are neglected. Thus, Eq. 5 is rewritten as follows:

$$\dot{\varepsilon} = \dot{\varepsilon}_{el} + \dot{\varepsilon}_{in} = \dot{\varepsilon}_{el} + \dot{\varepsilon}_{tr} \tag{22}$$

The transformation strain rate $\dot{\varepsilon}_{tr}$ is assumed to be proportional to the martensite fraction rate:

$$\dot{\varepsilon}_{tr} = \dot{f}_m \Delta\varepsilon_{tr} \tag{23}$$

The proportionality described in Eq. 23 is assumed to be valid in a zone between the beginning and end of phase transformation, i.e. in the "plateau". This zone experiences more intensely the formation of favorably orientend martensite variants, which form before less favorably oriented ones. Far from this zone, the proportionality described by Eq. 23 may not be respected.

5.2.2. Thermal power assumptions

The total thermal power is assumed to consist only of thermoelasticity and phase transformation. The dissipation power induced by plasticity ($\dot{q}_{pl}$) is neglected. With that, Eq. 6 is rewritten as follows:

$$\dot{q} = \dot{q}_{thel} + \dot{q}_{in} = \dot{q}_{thel} + \dot{q}_{tr} \tag{24}$$

where the thermal power due to phase transformation ($\dot{q}_{tr}$) is:

$$\dot{q}_{tr} = \dot{f} \Delta H_{tr} \tag{25}$$

The proportionality described in Eq. 25 is assumed to be valid throughout the whole phase transformation.

5.2.3. Determining the ratio $\frac{\dot{q}_{tr}}{\dot{\varepsilon}_{tr}}$

The following expression is obtained from Eqs. 22 to 25:

$$\frac{\dot{q}_{tr}}{\dot{\varepsilon}_{tr}} = \frac{\dot{q}_{in}}{\dot{\varepsilon}_{in}} = \frac{\dot{q} + \frac{\alpha T_0 \dot{\sigma}}{\rho}}{\dot{\varepsilon} - \frac{\dot{\sigma}}{E}} = \frac{\Delta H_{fr}(f_m)}{\Delta\varepsilon_{tr}} \tag{26}$$

All terms in the third part of Eq. 26 are obtained experimentally. The analysis of the ratio $\dot{q}_{in}/\dot{\varepsilon}_{in}$ is performed separately for the cyclic and rupture tests.

Cyclic Test

Figure 12 shows the ratio $\dot{q}_{in}/\dot{\varepsilon}_{in}$ as a function of total true strain for a cyclic tensile test. This ratio is constant during loading for strains higher than 1.8% and during unloading for strains between 1.8% and 3.6%. The values in the middle zone are rather constant. This behaviour agrees with the assumptions made in section 5.2.1, about Eq. 23 which are valid in a zone away from beginning/end of phase transformation.

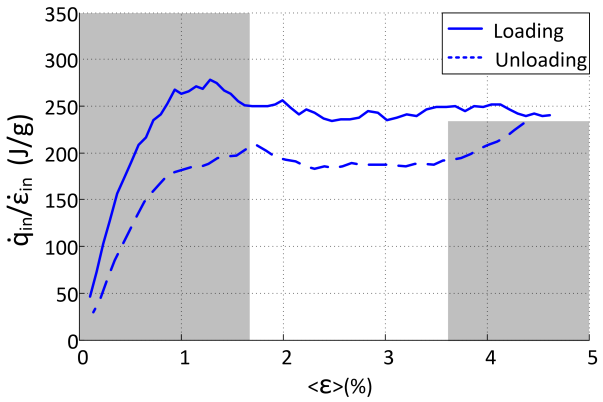

Figure 12: *Ratio $\dot{q}_{in}/\dot{\varepsilon}_{in}$, computed using experimental data and Eq. 26, as a function of true strain. The experimental error is ±5 J/g.*

Rupture test

Figure 13 presents the ratio $\dot{q}_{in}/\dot{\varepsilon}_{in}$ as a function of true strain (Fig. 13a) and nominal stress (Fig. 13b) for the tensile test until rupture. Similarly to the curve shown in Fig. 12, three distinct zones can be observed: two gray zones at the beginning and end of transformation, and a rather constant zone in the middle. This result again ratifies the hypothesis put forward in section 5.2.1 and the results shown in Fig. 12. The decrease in the ratio $\dot{q}_{in}/\dot{\varepsilon}_{in}$ after $\sim$ 7.5% and after $\sim$ 1200 MPa might be mostly associated with the plastic strain experienced before rupture.

Figure 14a shows the nominal stress and Fig. 14b shows the ratio $d\sigma/d\varepsilon$ as a function of true strain. Three zones can be observed in Fig. 14a: I - from 0% to $\sim$ 2%, II - from $\sim$ 2% to $\sim$ 7.5% and III - from $\sim$ 7.5% until rupture. Zone I

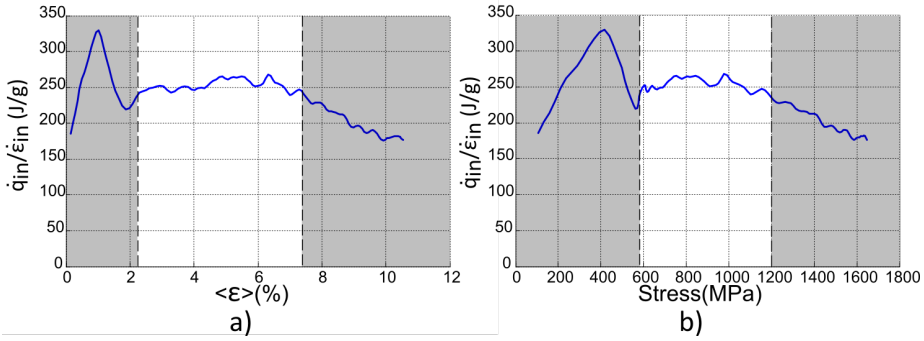

Figure 13: *Ratio $\dot{q}_{in}/\dot{\varepsilon}_{in}$ computed with Eq. 26 and experimental data from the rupture test as a function of a) strain and b) nominal stress.*

may be assumed as predominantly involving elastic deformation, while zone II mostly involves phase transformation. Finally, zone III presents the beginning of plastic deformation around $\sim 7.5\%$.

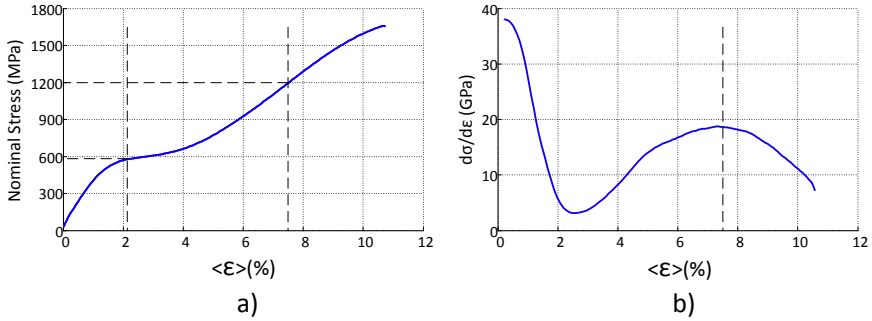

Figure 14: *a) Nominal stress-true strain. b) Ratio $d\sigma/d\varepsilon$ as a function of true strain.*

Figure 14 shows the evolution of the slope $d\sigma/d\varepsilon$ with true strain. This slope is not constant, which indicates that no pure elastic zone is present in the rupture tensile test. At the beginning of a SIPT, with the material in the austenite phase, the slope decreases during loading, reaching a minimum at about the middle of the stress "plateau". Then the slope increases until the end of phase transformation. Once plastic deformation is present and the slope $d\sigma/d\varepsilon$ again decreases with a further increase of strain. Based on this, the inflection point

around $\sim 7.5\%$ strain in Fig.14b indicates the beginning of plastic deformation. These results support the assumption that the zone between $\sim 2\%$ and $\sim 7.5\%$ strain predominantly contains phase transformation.

5.3. Determination of ΔH_{tr}

From the results obtained in section 5.2.3 and assuming that the ratio $\dot{q}_{tr}/\dot{\varepsilon}_{tr}$ is constant in the zone between $\sim 2\%$ and $\sim 7.5\%$ during loading and between 3.6% and 1.8% during unloading, Eq. 26 can be rewritten as:

$$\Delta H_{tr} = (\dot{q}_{tr}/\dot{\varepsilon}_{tr})\Delta\varepsilon_{tr} \tag{27}$$

The specific latent heat (ΔH_{tr}), calculated for both cyclic and rupture tests using Eq. 27 and the experimental data, are shown in Table 1.

Table 1: Mean specific latent heat values during loading and unloading for cyclic and rupture tests.

	Cyclic Test	Rupture Test
ΔH_{tr}^{A-M}	19.6 ± 0.4 J/g	$20.2 \pm 1.3 J/g$
ΔH_{tr}^{M-A}	14.9 ± 0.2 J/g	–

These results were obtained with a value of transformation strain $\Delta\varepsilon_{tr} = 8\%$ and in the [1.8%, 3.8%] strain interval for the cyclic test and between $\varepsilon = 2\%$ and 7.5% strain for the rupture test.

These values are comparable to those obtained by [45] from DSC measurements. The authors showed that for fully annealed NiTi alloys the specific latent heat values decrease from about 30 J/g to 10 J/g with an increase in at.%Ni. For a Ti-50.9at.%Ni alloy, the values obtained were around $17 J/g$ [46, 45].

5.4. Analysis of the difference between ΔH_{tr}^{A-M} and ΔH_{tr}^{M-A}

As shown in Eq. 12, the specific latent heat of transformation ΔH_{tr} of the SMA wire in tension consists of a enthalpy change ΔH_c, an elastic energy E_{st}

stored or released during the transformation process and a mechanical work $W'_{mech} = \frac{1}{\rho}\sigma\Delta\varepsilon_{tr}$. As shown in Eq. 19, the difference between forward and reverse transformation enthalpies (where $\Delta H_{tr}^{A-M} > \Delta H_{tr}^{M-A}$) is associated only with the mechanical energy (W'_{mech}). Rewriting Eq. 19 gives:

$$\Delta H_{tr}^{A-M} - \Delta H_{tr}^{M-A} = \frac{1}{\rho}\sigma^{A-M}\Delta\varepsilon_{tr} - \frac{1}{\rho}\sigma^{M-A}\Delta\varepsilon_{tr} \tag{28}$$

From the thermal analysis, the difference between specific latent heat on loading and unloading is $\Delta H_{tr}^{A-M} - \Delta H_{tr}^{M-A} = 4.7 \pm 0.6$ J/g. From a mechanical stand point, assuming σ^{A-M} as the mean stress of the forward transformation "plateau" and σ^{M-A} as the mean stress for the reverse transformation "plateau", the difference in mechanical energy between loading and unloading is $W'^{A-M}_{mech} - W'^{M-A}_{mech} = 3.5 \pm 0.7$ J/g. The mean stress values, as well as the standard deviation, were calculated between 1% and 1.5% transformation strain. The weak difference between these two experimental results (4.7 and 3.5 J/g) seems to confirm the theoretical relation in Eq. 19.

5.5. Estimation of martensite fraction (f_m)

The martensite fraction was obtained only for the cyclic test due to the absence of plastic effects. It was calculated by time integration of the martensite fraction rate deduced from Eq. 27, where $\dot{f}_m = \dot{q}_{tr}/\Delta H_{tr}$. The ΔH_{tr} values used are in the first column of Table 1.

Figure 15 shows the evolution of the martensite fraction as a function of (a) strain and (b) nominal stress. Loading can be identified by the solid line between 0% and point a in Fig. 15. The red-line delimited by points "a" and "b" corresponds to the hold time at the end of loading. The dashed lines represent the martensite fraction during unloading.

In Fig. 15a, the solid curve shows that $A - M$ phase transformation takes place from the beginning of strain, even before the superelastic "plateau". Likewise, in Fig. 15b during loading, around 5% of martensite is formed between 0 and 400 MPa and more than 10% at 600 MPa. Note that this amount of martensite is present in a strain range commonly considered to be purely elastic. This

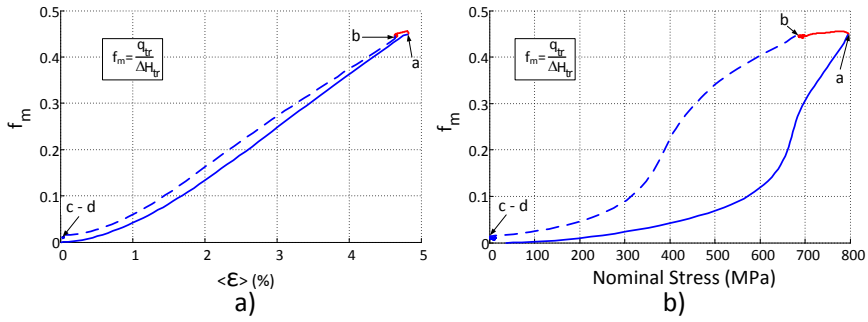

Figure 15: *a) Martensite fraction as a function of a) strain and b) nominal stress. The solid lines represent loading and dashed lines unloading.*

result is related to the early increasing amount of thermal power observed in Figs. 7, 8 and 10.

Between points "a" and "b" there is a modest decrease in the martensite fraction due to reverse transformation. It is related with the small stress decrease during this hold time, which in turn is associated with the relaxation caused by the temperature decrease. At the beginning of unloading (Fig. 15b), between point "b" and 500 MPa, around 10 % of martensite transforms into austenite. Furthermore, the path described by the martensite fraction in Fig. 15, where its value is higher during unloading than during loading, was also reported in the study of [47].

A maximum martensite fraction of $f_m = 0.45$ is achieved at the end of loading. This behaviour does not follow what was commonly assumed in literature, i.e. that at the end of superelastic "plateau" all the microstructure in the austenite phase had transformed into the martensite phase [48]. Indeed, recent studies using neutron diffraction to measure the crystal phase structure and determine the martensite fraction during stress induced phase transformation have shown that martensite fraction is below unit after the "plateau" [49, 47]. Authors in [49] obtained a maximum of $f_m = 0.95$ at $\varepsilon = 11\%$ strain in a stress relieved NiTi rod (Ti-50.8at.%Ni). Such high value for the martensite fraction is expected in stress relieved materials because the grain size tends to increase

with the heat treatment intensity, as well as the phase transformation intensity.

For nanostructured materials, however, numerous studies [12, 50, 51] reveal that the reduced grain size tends to partially suppress martensite phase transformation. It has been shown that the grain size reduction drastically decreases the grain's potential to be a nucleation site [52]. In the present study, the material used is assumed to have a nanoscale crystalline structure, since it was submitted to a severe cold work fabrication process and underwent a low magnitude heat treatment [9, 12] at temperatures below recrystallization. The manufacturing history associated with the absence of transformation peak on DSC curve [12] is in accordance with the low level of martensite fraction achieved, as seen in Fig. 15.

6. Conclusion

This study analyses the thermomechanical tensile behaviour of a cold drawn Ti-50.9at.%Ni wire subjected to heat treatment at 598 K for 30 min, which is below the grain growth and crystallization temperature (623 K). Such low heat treatment temperature induces a superelastic loop without a stress plateau. However, the absence or weakness of DSC peaks hampers the determination of specific latent heat. This is a common effect of nanostructured materials such as the superelastic wire used in the study. A method using strain and temperature field measurements was developed and used to determine thermal power and thermal energy during superelastic tensile tests through a heat balance. From these results and using a thermodynamic approach, forward and reverse specific latent heat and the martensite fraction as a function of strain and stress were estimated. The calculated specific latent heat values were 19.6 J/g for forward and 14.9 J/g for reverse transformation. A maximum of 45% martensite fraction was calculated when the global strain was limited to about 5%. We also calculated an increase from 0 to 5% of the martensite fraction between 0 and 400 MPa on loading, i.e. commonly considered to be an elastic region. Likewise, in a supposedly elastic zone at the beginning of unloading (between 680 MPa

and 500 MPa), around 10% of the martensite fraction was recovered. These results highlight the presence of phase transformation phenomenon throughout the superelastic cycle.

Acknowledgments

This work was conducted as part of a scholarship (248891/2013-8) supported by the Ciências Sem Fronteiras Program at the University of Grenoble, financed by the Brazilian National Council for Scientific and Technological Development (CNPq).

References

[1] A. Ahadi, E. Rezaei, A. Karimi Taheri, Effect of hot rolling on microstructure and transformation cycling behaviour of equiatomic NiTi shape memory alloy, Mater. Sci. and Technol. 28 (000) (2012) 727–732. doi:10.1179/1743284711Y.0000000130.
URL http://www.ingentaconnect.com/content/maney/mst/pre-prints/1743284711Y.0000000130

[2] R. Delville, B. Malard, J. Pilch, P. Sittner, D. Schryvers, Microstructure changes during non-conventional heat treatment of thin Ni–Ti wires by pulsed electric current studied by transmission electron microscopy, Acta Materialia 58 (13) (2010) 4503–4515. doi:10.1016/j.actamat.2010.04.046.
URL http://dx.doi.org/10.1016/j.actamat.2010.04.046http://linkinghub.elsevier.com/retrieve/pii/S1359645410002727

[3] M. E. Mitwally, M. Farag, Effect of cold work and annealing on the structure and characteristics of NiTi alloy, Materials Science and Engineering: A 519 (1-2) (2009) 155–166. doi:10.1016/j.msea.2009.04.057.
URL http://linkinghub.elsevier.com/retrieve/pii/S092150930900567X

[4] M. Peterlechner, J. Bokeloh, G. Wilde, T. Waitz, Study of relaxation and crystallization kinetics of NiTi made amorphous by repeated cold rolling, Acta Materialia 58 (20) (2010) 6637–6648. doi:10.1016/j.actamat.2010.08.026.
URL http://linkinghub.elsevier.com/retrieve/pii/S1359645410005409

[5] X. Shi, L. Cui, D. Jiang, C. Yu, F. Guo, M. Yu, Y. Ren, Y. Liu, Grain size effect on the R-phase transformation of nanocrystalline NiTi shape memory alloys, Journal of Materials Science 49 (13) (2014) 4643–4647. doi:10.1007/s10853-014-8167-6.
URL http://link.springer.com/10.1007/s10853-014-8167-6

[6] A. Sergueeva, C. Song, R. Valiev, A. Mukherjee, Structure and properties of amorphous and nanocrystalline NiTi prepared by severe plastic deformation and annealing, Materials Science and Engineering: A 339 (1-2) (2003) 159–165. doi:10.1016/S0921-5093(02)00122-3.
URL http://linkinghub.elsevier.com/retrieve/pii/S0921509302001223

[7] C. Yu, B. Aoun, L. Cui, Y. Liu, H. Yang, X. Jiang, S. Cai, D. Jiang, Z. Liu, D. E. Brown, Y. Ren, Synchrotron high energy X-ray diffraction study of microstructure evolution of severely cold drawn NiTi wire during annealing, Acta Materialia 115 (2016) 35–44. doi:10.1016/j.actamat.2016.05.039.
URL http://linkinghub.elsevier.com/retrieve/pii/S1359645416303901

[8] D. Favier, H. Louche, P. Schlosser, L. Orgéas, P. Vacher, L. Debove, Homogeneous and heterogeneous deformation mechanisms in an austenitic polycrystalline Ti-50.8 at.% Ni thin tube under tension. Investigation via temperature and strain fields measurements, Acta Materialia 55 (16) (2007) 5310–5322. doi:10.1016/j.actamat.2007.05.027.

[9] A. Ahadi, Q. Sun, Effects of grain size on the rate-dependent thermomechanical responses of nanostructured superelastic NiTi, Acta Materialia 76 (2014) 186–197. doi:10.1016/j.actamat.2014.05.007.

[10] C.-H. Li, L.-J. Chiang, Y.-F. Hsu, W.-H. Wang, Cold Rolling-Induced Multistage Transformation in Ni-Rich NiTi Shape Memory Alloys, MATERIALS TRANSACTIONS 49 (9) (2008) 2136–2140. doi:10.2320/matertrans.MER2008138.
URL http://joi.jlc.jst.go.jp/JST.JSTAGE/matertrans/MER2008138?from=CrossRef

[11] S. Chang, S. Wu, G. Chang, Transformation sequence in severely cold-rolled and annealed Ti50Ni50 alloy, Materials Science and Engineering: A 438-440 (2006) 509–512. doi:10.1016/j.msea.2006.02.124.
URL http://linkinghub.elsevier.com/retrieve/pii/S0921509306006095

[12] K. Tsuchiya, M. Inuzuka, D. Tomus, A. Hosokawa, H. Nakayama, K. Morii, Y. Todaka, M. Umemoto, Martensitic transformation in nanostructured TiNi shape memory alloy formed via severe plastic deformation, Materials Science and Engineering: A 438-440 (2006) 643–648. doi:10.1016/j.msea.2006.01.110.
URL http://linkinghub.elsevier.com/retrieve/pii/S0921509306006320

[13] D. a. Miller, D. C. Lagoudas, Influence of cold work and heat treatment on the shape memory effect and plastic strain development of NiTi, Materials Science and Engineering: A 308 (1-2) (2001) 161–175. doi:10.1016/S0921-5093(00)01982-1.
URL http://linkinghub.elsevier.com/retrieve/pii/S0921509300019821

[14] Q. Kan, C. Yu, G. Kang, J. Li, W. Yan, Experimental observations on rate-dependent cyclic deformation of super-elastic NiTi

shape memory alloy, Mechanics of Materials 97 (2016) 48–58. doi:10.1016/j.mechmat.2016.02.011.
URL http://dx.doi.org/10.1016/j.mechmat.2016.02.011http://linkinghub.elsevier.com/retrieve/pii/S0167663616000429

[15] J. Tušek, K. Engelbrecht, L. Mañosa, E. Vives, N. Pryds, Understanding the Thermodynamic Properties of the Elastocaloric Effect Through Experimentation and Modelling, Shape Memory and Superelasticity 2 (4) (2016) 317–329. doi:10.1007/s40830-016-0094-8.
URL http://link.springer.com/10.1007/s40830-016-0094-8

[16] M. Schmidt, S.-M. Kirsch, S. Seelecke, A. Schütze, S. Seelecke, Elastocaloric Cooling: from Fundamental Thermodynamics to Solid State Air Conditioning, Science and Technology for the Built Environment 22 (5) (2016) 475–488. doi:10.1080/23744731.2016.1186423.
URL http://www.tandfonline.com/doi/full/10.1080/23744731.2016.1186423

[17] S. Qian, Y. Geng, Y. Wang, J. Ling, Y. Hwang, R. Radermacher, I. Takeuchi, J. Cui, A review of elastocaloric cooling: Materials, cycles and system integrations, International Journal of Refrigeration 64 (2016) 1–19. doi:10.1016/j.ijrefrig.2015.12.001.
URL http://dx.doi.org/10.1016/j.ijrefrig.2015.12.001

[18] A. Chrysochoos, H. Louche, An infrared image processing to analyse the calorific effects accompanying strain localisation, International Journal of Engineering Science 38 (16) (2000) 1759–1788. doi:10.1016/S0020-7225(00)00002-1.
URL http://linkinghub.elsevier.com/retrieve/pii/S0020722500000021

[19] P. Schlosser, H. Louche, D. Favier, L. Orgéas, Image Processing to Estimate the Heat Sources Related to Phase Transformations during Tensile Tests of NiTi Tubes, Strain 43 (3) (2007) 260–271.

doi:10.1111/j.1475-1305.2007.00350.x.
URL http://hal.archives-ouvertes.fr/hal-00180898/en/http://doi.wiley.com/10.1111/j.1475-1305.2007.00350.x

[20] V. Delobelle, D. Favier, H. Louche, Heat Estimation from Infrared Measurement Compared to DSC for Austenite to R Phase Transformation in a NiTi Alloy, Journal of Materials Engineering and Performance 22 (6) (2013) 1688–1693. doi:10.1007/s11665-012-0466-y.
URL http://link.springer.com/10.1007/s11665-012-0466-y

[21] V. Delobelle, D. Favier, H. Louche, N. Connesson, Determination of Local Thermophysical Properties and Heat of Transition from Thermal Fields Measurement During Drop Calorimetric Experiment, Experimental Mechanics 55 (4) (2015) 711–723. doi:10.1007/s11340-014-9877-z.
URL http://link.springer.com/10.1007/s11340-014-9877-z

[22] B. Malard, J. Pilch, P. Sittner, R. Delville, C. Curfs, In situ investigation of the fast microstructure evolution during electropulse treatment of cold drawn NiTi wires, Acta Materialia 59 (4) (2011) 1542–1556. doi:10.1016/j.actamat.2010.11.018.
URL http://dx.doi.org/10.1016/j.actamat.2010.11.018

[23] B. Malard, J. Pilch, P. Sittner, V. Gartnerova, R. Delville, D. Schryvers, C. Curfs, Microstructure and functional property changes in thin NiTi wires heat treated by electric current - High energy X-ray and tem investigations, Functional Materials Letters 2 (2) (2009) 45–54. doi:10.1142/S1793604709000557.

[24] A. Ahadi, Q. Sun, Stress-induced nanoscale phase transition in superelastic NiTi by in situ X-ray diffraction, Acta Materialia 90 (2015) 272–281. doi:10.1016/j.actamat.2015.02.024.
URL http://dx.doi.org/10.1016/j.actamat.2015.02.024

[25] S. Prokoshkin, V. Brailovski, K. Inaekyan, V. Demers, a. Kreitcberg,

Nanostructured Ti–Ni Shape Memory Alloys Produced by Thermomechanical Processing, Shape Memory and Superelasticity 1 (2) (2015) 191–203. doi:10.1007/s40830-015-0026-z.
URL http://link.springer.com/10.1007/s40830-015-0026-z

[26] V. Delobelle, G. Chagnon, D. Favier, T. Alonso, Study of electropulse heat treatment of cold worked NiTi wire: From uniform to localised tensile behaviour, Journal of Materials Processing Technology 227 (2016) 244–250. doi:10.1016/j.jmatprotec.2015.08.011.
URL http://dx.doi.org/10.1016/j.jmatprotec.2015.08.011

[27] P. Schlosser, Influence of thermal and mechanical aspects on deformation behaviour of NiTi alloys, Ph.D. thesis, Université Joseph Fourier de Grenoble (2008).

[28] P. Leo, T. Shield, O. Bruno, Transient heat transfer effects on the pseudoelastic behavior of shape-memory wires, Acta Metallurgica et Materialia 41 (8) (1993) 2477–2485. doi:10.1016/0956-7151(93)90328-P.

[29] A. Chrysochoos, H. Pham, O. Maisonneuve, Energy balance of thermoelastic martensite transformation under stress, Nuclear Engineering and Design 162 (1) (1996) 1–12. doi:10.1016/0029-5493(95)01140-4.
URL http://linkinghub.elsevier.com/retrieve/pii/0029549395011404

[30] H. Martinni Ramos de Oliveira, Study of thermomechanical couplings in nanostructured superelastic nickel-titanium wires, Ph.D. thesis, Université Grenoble Alpes, France. (2018).

[31] X. Balandraud, E. Ernst, E. Soos, Monotone strain-stress models for shape memory alloys hysteresis loop and pseudoelastic behaviorx, Zeitschrift fÜr angewandte Mathematik und Physik 56 (2) (2005) 304–356. doi:10.1007/s00033-004-2026-2.
URL http://www.springerlink.com/index/10.1007/

s00033-004-2026-2http://link.springer.com/10.1007/s00033-004-2026-2

[32] P. Šittner, M. Landa, P. Lukáš, V. Novák, R-phase transformation phenomena in thermomechanically loaded NiTi polycrystals, Mechanics of Materials 38 (5-6) (2006) 475–492. doi:10.1016/j.mechmat.2005.05.025.

[33] L. C. Brinson, I. Schmidt, R. Lammering, Stress-induced transformation behavior of a polycrystalline NiTi shape memory alloy: Micro and macromechanical investigations via in situ optical microscopy, Journal of the Mechanics and Physics of Solids 52 (7) (2004) 1549–1571. doi:10.1016/j.jmps.2004.01.001.

[34] T. Alonso, D. Favier, G. Chagnon, Characterizing transformation phenomena and elastic moduli of austenite and oriented martensite of superelastic thin NiTi wire through isothermal Dynamic Mechanical Analysis, Journal of Materials Engineering and Performance (2019) 2–28doi:10.1002/ente.20)).

[35] R. Zaera, J. A. Rodríguez-Martínez, D. Rittel, On the Taylor-Quinney coefficient in dynamically phase transforming materials. Application to 304 stainless steel, International Journal of Plasticity 40 (2013) 185–201. doi:10.1016/j.ijplas.2012.08.003.
URL http://dx.doi.org/10.1016/j.ijplas.2012.08.003

[36] R. Zaera, J. A. Rodríguez-Martínez, A. Casado, J. Fernández-Sáez, A. Rusinek, R. Pesci, A constitutive model for analyzing martensite formation in austenitic steels deforming at high strain rates, International Journal of Plasticity 29 (1) (2012) 77–101. doi:10.1016/j.ijplas.2011.08.003.
URL http://dx.doi.org/10.1016/j.ijplas.2011.08.003

[37] D. Rittel, On the conversion of plastic work to heat during high strain rate deformation of glassy polymers, Mechanics of Materials 31 (2) (1999) 131–139. doi:10.1016/S0167-6636(98)00063-5.

[38] R. Peyroux, A. Chrysochoos, C. Licht, M. Löbel, THERMOMECHANICAL COUPLINGS AND PSEUDOELASTICITY OF SHAPE MEMORY ALLOYS, International Journal of Engineering Science 36 (4) (1998) 489–509. doi:10.1016/S0020-7225(97)00052-9.
URL http://www.sciencedirect.com/science/article/pii/S0020722597000529http://linkinghub.elsevier.com/retrieve/pii/S0020722597000529

[39] J. Ortín, A. Planes, Thermodynamic analysis of thermal measurements in thermoelastic martensitic transformations, Acta Metallurgica 36 (8) (1988) 1873–1889. doi:10.1016/0001-6160(88)90291-X.
URL http://linkinghub.elsevier.com/retrieve/pii/000161608890291X

[40] J. Ortín, A. Planes, Thermodynamics of thermoelastic martensitic transformations, Acta Metallurgica 37 (5) (1989) 1433–1441. doi:10.1016/0001-6160(89)90175-2.
URL http://linkinghub.elsevier.com/retrieve/pii/0001616089901752

[41] J. Ortín, A. Planes, THERMODYNAMICS AND HYSTERESIS BEHAVIOUR OF THERMOELASTIC MARTENSITIC TRANSFORMATIONS, Le Journal de Physique IV 01 (C4) (1991) C4–13–C4–23. doi:10.1051/jp4:1991402.
URL http://www.edpsciences.org/10.1051/jp4:1991402

[42] P. Wollants, J. Roos, L. Delaey, Thermally- and stress-induced thermoelastic martensitic transformations in the reference frame of equilibrium thermodynamics, Progress in Materials Science 37 (3) (1993) 227–288. doi:10.1016/0079-6425(93)90005-6.
URL http://linkinghub.elsevier.com/retrieve/pii/0079642593900056

[43] L. Orgéas, D. Favier, Stress-induced martensitic transformation of a NiTi

alloy in isothermal shear, tension and compression, Acta Materialia 46 (15) (1998) 5579–5591. doi:10.1016/S1359-6454(98)00167-0.
URL http://linkinghub.elsevier.com/retrieve/pii/S1359645498001670

[44] S. Miyazaki, S. Kimura, K. Otsuka, Y. Suzuki, The habit plane and transformation strains associated with the martensitic transformation in Ti-Ni single crystals, Scripta Metallurgica 18 (9) (1984) 883–888. doi:10.1016/0036-9748(84)90254-0.
URL http://linkinghub.elsevier.com/retrieve/pii/0036974884902540

[45] J. Frenzel, A. Wieczorek, I. Opahle, B. Maaß, R. Drautz, G. Eggeler, On the effect of alloy composition on martensite start temperatures and latent heats in Ni–Ti-based shape memory alloys, Acta Materialia 90 (2015) 213–231. doi:10.1016/j.actamat.2015.02.029.
URL http://www.sciencedirect.com/science/article/pii/S1359645415001299

[46] J. Khalil-Allafi, B. Amin-Ahmadi, The effect of chemical composition on enthalpy and entropy changes of martensitic transformations in binary NiTi shape memory alloys, Journal of Alloys and Compounds 487 (1-2) (2009) 363–366. doi:10.1016/j.jallcom.2009.07.135.
URL http://linkinghub.elsevier.com/retrieve/pii/S0925838809014881

[47] A. R. Pelton, B. Clausen, A. P. Stebner, In Situ Neutron Diffraction Studies of Increasing Tension Strains of Superelastic Nitinol, Shape Memory and Superelasticity 1 (3) (2015) 375–386. doi:10.1007/s40830-015-0031-2.
URL http://link.springer.com/10.1007/s40830-015-0031-2

[48] D. C. Lagoudas, Shape Memory Alloys, Texas, USA, 2008.

[49] A. P. Stebner, H. M. Paranjape, B. Clausen, L. C. Brinson, A. R. Pelton, In Situ Neutron Diffraction Studies of Large Monotonic Deformations of

Superelastic Nitinol, Shape Memory and Superelasticity 1 (2) (2015) 252–267. doi:10.1007/s40830-015-0015-2.
URL http://link.springer.com/10.1007/s40830-015-0015-2

[50] T. Waitz, K. Tsuchiya, T. Antretter, F. D. Fischer, Phase Transformations of Nanocrystalline Martensitic Materials, MRS Bulletin 34 (11) (2009) 814–821. doi:10.1557/mrs2009.231.

[51] A. Glezer, E. Blinova, V. Pozdnyakov, A. Shelyakov, Martensite Transformation in Nanoparticles and Nanomaterials, Journal of Nanoparticle Research 5 (5/6) (2003) 551–560. doi:10.1023/B:NANO.0000006094.08917.46.
URL http://link.springer.com/10.1023/B:NANO.0000006094.08917.46

[52] I.-W. Chen, Y.-H. Chiao, K. Tsuzaki, Statistics of martensitic nucleation, Acta Metallurgica 33 (10) (1985) 1847–1859. doi:10.1016/0001-6160(85)90007-0.
URL http://linkinghub.elsevier.com/retrieve/pii/0001616085900070